



## Anchoring titanium dioxide on carbon spheres for high-performance visible light photocatalysis

Haoyi Wu<sup>a</sup>, Xiao-Li Wu<sup>a,b</sup>, Zheng-Ming Wang<sup>a,\*</sup>, Hiroshi Aoki<sup>a</sup>, Shuzo Kutsuna<sup>a</sup>, Keiko Jimura<sup>c</sup>, Shigenobu Hayashi<sup>c</sup>

<sup>a</sup> Environmental Management Research Institute, National Institute of Advanced Industrial Science and Technology, 16-1 Onogawa, Tsukuba, Ibaraki, 305-8569, Japan

<sup>b</sup> College of Architecture and Environment, Sichuan University, No. 24 South Section 1, Yihuan Road, Chengdu, 610065, Sichuan, PR China

<sup>c</sup> Research Institute for Material and Chemical Measurement, National Institute of Advanced Industrial Science and Technology, 1-1-1 Higashi, Tsukuba, Ibaraki, 305-8565, Japan



### ARTICLE INFO

#### Article history:

Received 17 October 2016

Received in revised form

14 December 2016

Accepted 7 February 2017

Available online 8 February 2017

#### Keywords:

Titania

Carbon microsphere

Core–shell structure

Visible light photocatalyst

### ABSTRACT

The interfacing carbon materials can improve the visible light absorption of titanium dioxide ( $\text{TiO}_2$ ). Here  $\text{TiO}_2$  was anchored on carbon spheres (CSs) obtained by the hydrothermal polymerization of sucrose to bathochromically expand its light-response region. Nano- $\text{TiO}_2$  is condensed on the CS surface upon hydrothermal treatment to generate a core–shell structure ( $\text{TiO}_2@CS$ ). Because of interface formation between the two materials,  $\text{TiO}_2@CS$  achieved an enhanced visible light absorption compared to pure  $\text{TiO}_2$ . In addition, it degraded organic pollutants, such as methyl orange, bisphenol A, and Oseltamivir, more efficiently than pure  $\text{TiO}_2$  and the well-known graphene–P25  $\text{TiO}_2$  nanocomposite under visible light irradiation. This promoted visible light photoactivity was evidenced by the enhanced photocurrent responses and structure-dependent changes of electron spin resonance spectra that disclosed the critical role of an interfacial structure containing a doping level formed by tuning electrons from CS to  $\text{TiO}_2$ . Therefore, the facile hydrothermal formation of  $\text{TiO}_2@CS$  reveals new avenues for cost-effective ultraviolet-free photocatalysts exhibiting high efficiency.

© 2017 Elsevier B.V. All rights reserved.

## 1. Introduction

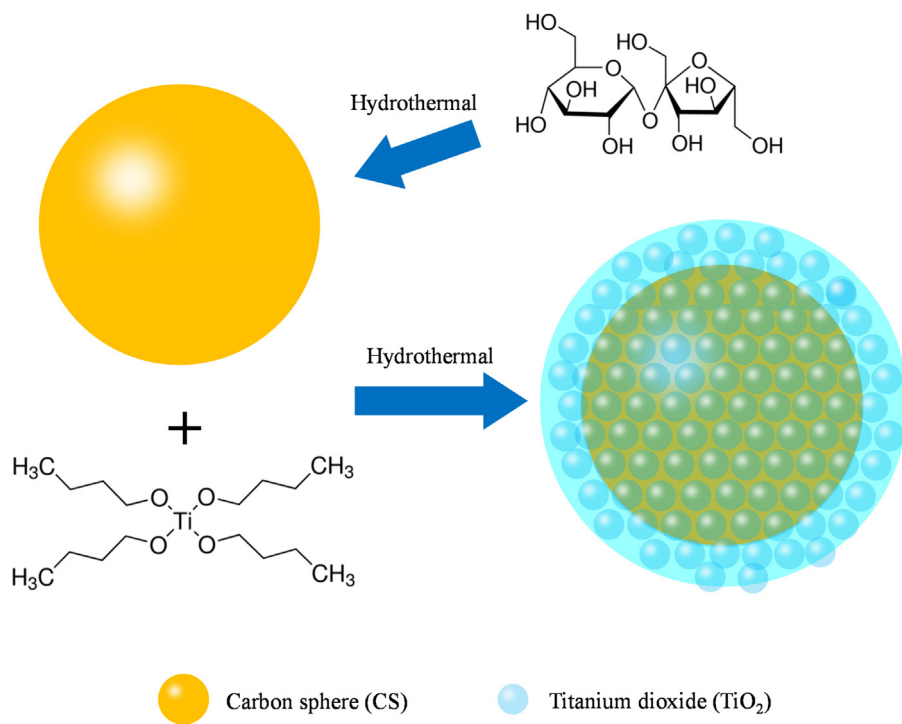
Since the discovery of its ability to promote the photolysis of water in 1972 [1], titanium dioxide ( $\text{TiO}_2$ ) has attracted tremendous research interest in the fields of chemistry, materials, energy, and environmental science. The excitation of  $\text{TiO}_2$  by a photon with sufficient energy generates electrons and holes in the conduction band (CB) and valence band (VB), respectively. These charge carriers react with  $\text{H}_2\text{O}$ ,  $\text{O}_2$ , and other organic species to form hydroxyl radicals ( $\cdot\text{OH}$ ) and superoxide radicals ( $\cdot\text{O}_2^-$ ), facilitating many photoinduced reactions such as water splitting and organic pollutant decompositions [2–9]. However,  $\text{TiO}_2$  exhibits a wide band gap (3.2 eV for anatase), which limits photoexcitation wavelengths needed to activate these reactions to ultraviolet (UV) light ( $\lambda < \sim 400 \text{ nm}$ ). Because UV light represents 3%–5% of the solar radiative energy, the majority of the solar energy is superfluous

and thus is wasted when  $\text{TiO}_2$ -catalyzed photoreaction is carried out under solar energy excitation. Prompting significant efforts to endow  $\text{TiO}_2$  with visible light photoactivity by widening its light absorption range toward visible light wavelengths has been a challenging requirement [10–12]. Wide-spectrum photocatalysts active from UV to visible light wavelengths are also expected to find use in various UV-free applications. For instance, the photocatalysts can be used in indoor environment remediation, where common incandescent lamps or energy-saving light-emitting diodes are employed to avoid damage of human skin and eyes by harmful UV, and in clothing materials inside which Mie scattering from cloth fibers tend to cut UV light.

Doping using nonmetals (C, N, or S) in  $\text{TiO}_2$ , metal or plasmonic nanoparticle deposition on  $\text{TiO}_2$ , dye-sensitizer employment, and semiconductor coupling have been attempted to achieve visible light-activated photocatalysis using  $\text{TiO}_2$  [3,7,8]. In particular, combining  $\text{TiO}_2$  with carbon materials has been proven to be an effective way to improve its visible light absorption ability [13–27]. For example, Zhang et al. synthesized graphene–P25  $\text{TiO}_2$  composite in a one-step hydrothermal reaction [28]. Petronella et al.

\* Corresponding author.

E-mail address: [zm-wang@aist.go.jp](mailto:zm-wang@aist.go.jp) (Z.-M. Wang).



**Scheme 1.** Schematic illustration on synthesis approach of  $\text{TiO}_2@\text{CS}$ .

directly grew  $\text{TiO}_2$  on carbon nanotubes (CNTs) [29]. Long et al. incorporated  $\text{C}_{60}$  into  $\text{TiO}_2$  by hydrothermal reaction [30]. These composite materials degraded organic pollutants more significantly than pure titania under visible light irradiation. However, the utilization of nano-carbons such as graphene, CNT, and  $\text{C}_{60}$  usually causes high cost and sometimes toxic issues.

In 2004, Sun et al. derived a colloidal carbon sphere (CS) exhibiting a highly hydrophilic surface by hydrothermal carbonization (HTC) of glucose. This carbon sphere served as a substrate for the immobilization or encapsulation of noble metal particles, such as Au, Ag, and Pt. It also acted as a template for the formation of hollow spherical shell structures [31]. Low cost and biocompatibility make CS a cost-effective and environmental friendly precursor applicable for various energy storing and environmental purposes [32–38]. A few recent studies have led to  $\text{TiO}_2$ -loaded CS, albeit under harsh preparation conditions such as low pH or high temperature pyrolysis. In addition, these composites presented greater photocatalytic activity than pure  $\text{TiO}_2$  under UV irradiation [39,40]. Zhao et al. constructed a spherical structure by one-pot hydrothermal treatment (HTT) of furfural and titanium precursor. In this structure,  $\text{TiO}_2$  and carbon moieties are contacted like brick and mortar, which endowed the materials with a visible light activity by the so-called dyad-type charge transfer mechanism [23]. Zhuang et al. modified this synthesis using surfactants to produce a similar but hollow  $\text{TiO}_2$ -C spherical shell with an open mouth, which showed a higher photocatalytic activity than its solid counterpart [24].

Here an ultrathin  $\text{TiO}_2$  shell of nanosize thickness was anchored over the CS core surface by a facile hydrothermal treatment, giving rise to an efficient visible light-driven photocatalyst toward the degradation of organic pollutants. The core–shell structure  $\text{TiO}_2@\text{CS}$  produced by this simple but effective and inexpensive approach achieved considerably higher photoactivity than pure  $\text{TiO}_2$  and the graphene–P25 nanocomposite. Detailed photocurrent and electron spin resonance (ESR) analyses elucidated the structure-based sophisticated charge transfer mechanism explaining this enhanced photoactivity. These findings proved that the

unusual  $\text{TiO}_2$ –CS interfacial structure played a critical role in the visible light photocatalysis.

## 2. Materials and methods

### 2.1. CS synthesis

Carbon spheres were synthesized by a hydrothermal method. Typically, sucrose (1.368 g, Wako, JIS Special Grade) was dissolved in aqueous solution (20 mL) by ultrasonic treatment for 2 min. The solution was transferred to a 25 mL Teflon container, which was sealed in a stainless steel autoclave and subjected to hydrothermal treatment at 448 K for 4 h. After cooling down to room temperature, the powdered product in the treated solution was collected by centrifugation and washed sufficiently with distilled water. The wet powdered product was transferred using 11.65 mL distilled water to a glass vial to form a CS dispersion (solution A) with a concentration of  $5 \text{ mg L}^{-1}$ . The powdered product of CS was also obtained after drying at 323 K overnight.

### 2.2. Fabrication of CS- $\text{TiO}_2$ core–shell structure ( $\text{TiO}_2@\text{CS}$ )

Titanium (IV) Tetrabutoxide monomer ( $\text{Ti(OBu)}_4$ ) (Wako Special Grade) was selected as the  $\text{TiO}_2$  precursor. First, a determined volume of  $\text{Ti(OBu)}_4$  was added to 15 mL ethanol (EtOH, Wako, JIS Special Grade) under stirring to form a light yellow solution B and the solution was kept stirring for 2 min. Next, a certain amount of solution A was added into solution B under stirring and the mixture was kept stirring for another 2 min. The mixture was then poured into a 25 mL Teflon container which was sealed in a stainless steel autoclave and subjected to hydrothermal treatment at 433 K for 3 h. (refer to Supporting Information, Section 2 for the relationship of synthesizing temperature and photocatalytic activity). After cooling down to room temperature, the powdered product was collected by centrifugation, sufficiently washed with both distilled water and EtOH, and finally dried at 323 K overnight. The obtained  $\text{TiO}_2@\text{CS}$  samples are denoted as  $\text{CST}_n$  where  $n$  stands for the vol-

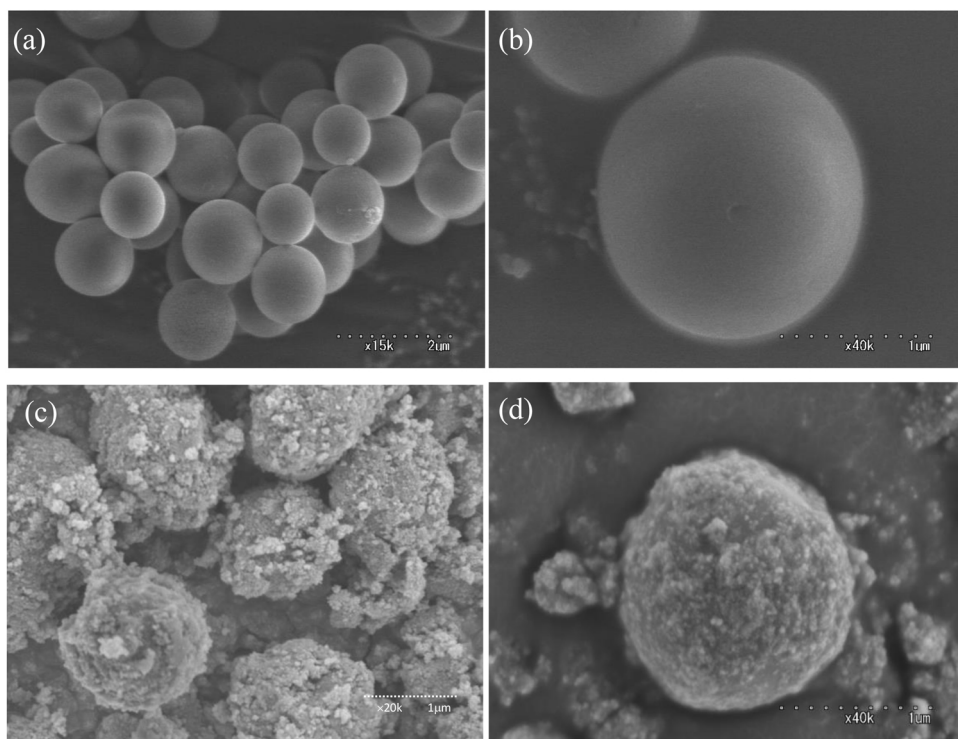


**Fig. 1.** SEM images of (a, b) CS and (c, d) CST3.

ume ratio of CS solution ( $5 \text{ mg L}^{-1}$ ) to the pure  $\text{Ti(OBu)}_4$  in synthesis whose detailed conditions are listed in Table S1. Syntheses were also carried out at different hydrothermal temperature and water content (Table S2) in which other conditions in the above procedure were maintained the same except that the examined condition was changed. In addition, a control sample, denoted as  $\text{TO}_3$ , was prepared by the same procedure and at same conditions as those of CST3 except that CS solution was replaced by distilled water. Details for the synthesis of the reference graphene- $\text{TiO}_2$  composite ( $\text{GT}_x$ ) are referred to in Section 2 of Supporting Information.

### 2.3. Materials characterizations

The crystal structure of the materials was determined using a Rigaku SmartLab diffractometer with  $\text{K}\alpha$  irradiation ( $\lambda = 0.15406 \text{ nm}$ ) at  $30 \text{ mA}$  and  $40 \text{ kV}$ . The Fourier Transform Infrared (FT-IR) spectra were measured using a Nicolet Nexus 470 Fourier Transform Infrared spectrometer with 200 scans at a resolution of  $2 \text{ cm}^{-1}$ .

The X-ray Photoelectron Spectroscopy (XPS) spectra were obtained on an ULVAC-PHI 5000 Versa Probe type instrument with an  $\text{Al K}\alpha$  irradiation ( $15 \text{ kV}$ ,  $25 \text{ W}$ , beam diameter:  $0.1 \text{ mm}$ ) and a neutralizer using argon ions and electron beams. The Ultraviolet and Visible Diffuse Reflectance spectra (UV-vis DRS) were recorded by a JASCO V-650 type UV-vis spectrometer. Thermogravimetric analysis (TG) of the materials was carried out by a Regaku Thermo plus TG8120-type analyzer under air atmosphere.

Morphology observation was done by a Hitachi S-4300 type field emission scanning electron microscope (FE-SEM) at an electron acceleration voltage of  $1 \text{ keV}$ . TEM observation together with selected area electronic diffraction (SAED) pattern and EDX spectrum analysis were carried out by a FEI Tecnai Osiris-type transmission electron microscope which is equipped with a high-angle annular dark field scanning TEM mode (HAADF-STEM). The electron acceleration voltage was  $200 \text{ keV}$ . The  $\text{N}_2$  adsorption-

desorption isotherms were collected at  $77 \text{ K}$  on a Belsorp Co.-made Belmax-type volumetric apparatus.

$^{13}\text{C}$  magic-angle-spinning (MAS) Nuclear Magnetic Resonance (NMR) spectra were measured with Bruker Avance III HD 600WB spectrometer at Larmor frequency of  $150.97 \text{ MHz}$ . A Bruker MAS probehead was used with a zirconia rotor of a  $4.0\text{-mm}$  outer diameter. The pulse sequence used was cross polarization (CP) with  $^1\text{H}$  high-power decoupling during signal acquisition. The flip angle of the initial  $^1\text{H}$  pulse was  $\pi/2$ , the contact time was  $2 \text{ ms}$ , and the repetition time was  $5 \text{ s}$ . The spinning rates of the sample were set at  $8$  and  $10 \text{ kHz}$ . The chemical shift scale was expressed with respect to neat tetramethylsilane (TMS) by adjusting the carboxyl signal of glycine spinning at  $8.0 \text{ kHz}$  to  $176.46 \text{ ppm}$ .

Electron Spin Resonance (ESR) spectra were recorded at  $77 \text{ K}$  by means of an X-band ESR spectrometer (JES-TE300, JEOL, Tokyo, Japan) under the following conditions: frequency,  $9.2 \text{ GHz}$ ; microwave power,  $1 \text{ mW}$ ; modulation frequency,  $100 \text{ kHz}$ ; magnetic field,  $326.5 \pm 10 \text{ mT}$ . Each powder sample was sealed in an ESR quartz tube without further evacuation and the measurements were carried out in ambient air.  $g$ -values were calibrated by comparison with the standard  $\text{Mn}^{2+}/\text{MgO}$  marker. A Xe lamp (Max-303, Asahi Bunko Co.) without and with a  $400 \text{ nm}$  cut-off filter was employed as the excitation source of full spectrum and visible light, respectively.

### 2.4. Photocatalytic experiments

The photocatalytic activity was examined by using MO, BPA and OP as the target organic pollutants. The initial concentrations ( $C_0$ ) of the starting solutions are  $1 \text{ mg L}^{-1}$  for MO and  $5 \text{ mg L}^{-1}$  for BPA and OP. In each photocatalytic experiment,  $20 \text{ mg}$  photocatalyst was added in  $100 \text{ mL}$  MO or  $50 \text{ mL}$  BPA or OP in a glass vessel and further dispersed by sonication for  $2 \text{ min}$ . Then the glass vessel was capped with a quartz cover and placed beneath a simulated solar light source (Jasco BS-300 type Xe lamp,  $300 \text{ W}$ ) with the liquid surface  $13 \text{ cm}$  apart from to assure an illuminance of  $0.15 \text{ W/cm}^2$ .

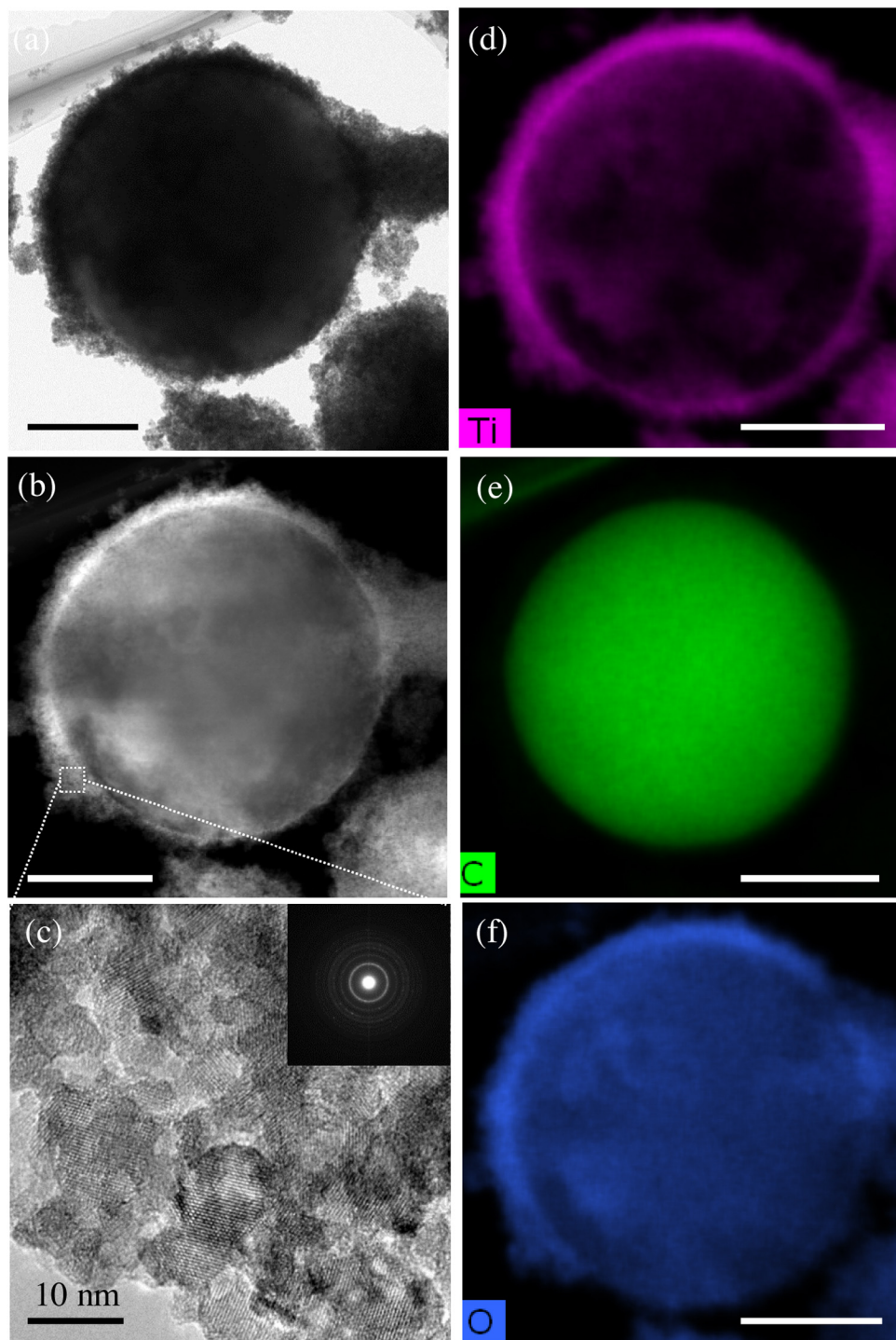


**Fig. 2.** (a) Dark field and (b) HADDF STEM images, (c) a high resolution expansion of an external portion of the  $\text{TiO}_2$  shell with a SAD inset, and elemental mapping images of (d) Ti, (e) C, and (f) O of a core-shell sphere of CST3.

on the top of the solution. The temperature of the reactor was controlled to be  $298 \pm 2$  K in a water bath during the reaction. Prior to illumination, the suspension was magnetically stirred in dark for 1 h to achieve adsorption equilibrium. Full spectrum solar light and visible light illuminations were carried out without and with a 400 nm cut-off filter, respectively. About 1 mL supernatant solution was sampled with a polytetrafluoroethylene filter (0.45  $\mu\text{m}$ , Membrane Solution Co. Ltd, Japan) at different time intervals and the concentrations were analyzed using a JASCO V-650 type UV-vis spectrometer for BPA and a Shimadzu Prominence high performance liquid chromatography (HPLC) system for MO and OP which

consists of two liquid pumps of Model LC-20AD, a DGU-20A3 type degasser, a SIL-20AC type auto sampler, a CTO-20AC type column oven, and a SPD-M20A diode array detector. The limit of quantification of MO for the HPLC equipment was determined to be 10  $\mu\text{g/L}$  with a relative standard deviation of 4%.

#### 2.5. Photocurrent measurement

Photocurrent measurement was carried out by chronoamperometry using a CHI Model 760AC electrochemical station (CHI Instrument). A 3-electrode system was employed, which uses Pt

wire as the counter electrode, Ag/AgCl aq. as the reference electrode, and a  $0.5 \text{ mol L}^{-1}$   $\text{Na}_2\text{SO}_4$  aqueous solution as the electrolyte. The working electrodes were prepared by spreading photocatalysts on fluorine doped tin oxide (FTO)-coated glass plates with the following procedure. Typically, 2 mg photocatalyst powder was dispersed in 2 mL EtOH under ultrasonic condition, following which a small amount of the dispersion was drop-casted on the electrode surface. After evaporation of ethanol, this procedure was repeated until all the materials were coated on the electrode. Both a simulated solar light source (JASCO BS-300 type Xe lamp, 300 W) and a light generator available for variable wavelength in the range of 390–700 nm with a resolution of 20 nm (Hamamatsu Photonics K.K.-made OSG type) were employed as the excitation source.

### 3. Results and discussion

#### 3.1. Structures of CS and $\text{TiO}_2@\text{CS}$

The  $\text{TiO}_2@\text{CS}$  core–shell structure was prepared in two steps (Scheme 1). First, CS was obtained via HTC of sucrose under similar conditions to those involving glucose as a precursor [31,32]. The carbonization gave spherical carbon particles (Fig. 1) with a sharp diameter distribution centered around  $1.1 (\pm 0.3) \mu\text{m}$  (Fig. S1). Second, CS (5 mg per liter water) was added to titanium (IV) tetrabutoxide ( $\text{Ti(OBu)}_4$ ) in ethanol at a CS/ $\text{Ti(OBu)}_4$  volume ratio  $n$  (Table S1) and the resulting mixture was subjected to HTT. During this second hydrothermal process,  $\text{TiO}_2$  nanoparticles were condensed on the CS surface to generate the composite CST $n$ , which displayed the  $\text{TiO}_2@\text{CS}$  core–shell structure. Upon  $\text{TiO}_2$  deposition and condensation, CST3 retained the spherical shape of the bare CS but exhibited a rougher surface (Fig. 1 and S2a–d). In contrast, the  $\text{TiO}_2$  control sample prepared without CS (TO3) comprised  $\text{TiO}_2$  nanoparticle aggregates but did not present a specific morphology (Fig. S2e). The core–shell structure was further evidenced by high-resolution transmission electron microscopy (HRTEM). Dark-field and high-angle annular dark field (HADDF) scanning transmission electron microscopy (STEM) images (Fig. 2a and b) clearly showed a shell surrounding a sphere. Elemental mapping images confirmed that the core mainly comprised carbon with the distribution of oxygen while the shell comprised titanium and oxygen (Fig. 2d–f and S2f for energy dispersive X-ray (EDX) of the entire area). HRTEM images of the shell displayed nanoparticles with the (001) lattice fringes typical of anatase (Fig. 2c), indicating that the shell comprised nanosized anatase crystal aggregates (see also the XRD patterns of CST $n$ , Fig. S3). The  $\text{TiO}_2@\text{CS}$  structure was found dependent on temperature, CS/Ti ratio ( $n$  value), and water content used during synthesis. The hydrothermal temperature primarily influences the crystallinity of  $\text{TiO}_2$  and a threshold temperature of 418 K is required to obtain anatase-type  $\text{TiO}_2$  (Fig. S4). When the CS/ $\text{Ti(OBu)}_4$  ratio (or the  $n$  of CST $n$ ) increased, the  $\text{TiO}_2$  content in the shell of CST $n$  decreased monotonously (Section 1 of Supporting Information and Fig. S5), progressively making the shell thinner and producing more cracks in the shell or uncovered parts on the CS surface (Fig. S6 and S7). Synthesis conditions without water did not form a clear shell structure because of less amount of  $\text{TiO}_2$  (Table S2 and Fig. S8). This suggests that the water content plays a crucial role in promoting the hydrolysis of  $\text{Ti(OBu)}_4$ , which contributes to the increase in the  $\text{TiO}_2$  building component amount required for the shell formation.

#### 3.2. FT-IR, XPS, NMR, and $\text{N}_2$ porosimetry

The  $\text{TiO}_2@\text{CS}$  structure was further characterized by FT-IR, XPS, and NMR techniques. The FT-IR spectrum of CS exhibited typical bands inherited from the sucrose precursor and was very similar to

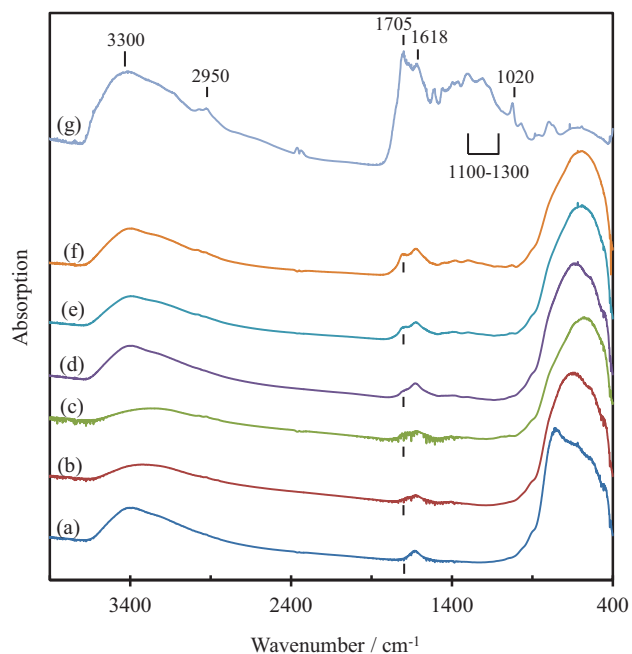


Fig. 3. FT-IR spectra of (a) TO3, CST $n$  with  $n =$  (b) 1, (c) 3, (d) 6, (e) 12, and (f) 24, and (g) CS.

that observed for its glucose-derived analogue [31]. It presented  $\text{C}=\text{C}$ , carboxyl ( $-\text{COOH}$ ), hydroxyl ( $-\text{OH}$ ), and epoxyl ( $\text{C}-\text{O}-\text{C}$ ) groups at  $1618$ ,  $1705$ ,  $1100$ – $1300$ , and  $1020 \text{ cm}^{-1}$ , respectively (Fig. 3). Moreover, bands attributed to  $\text{C}-\text{C}$  stretching,  $\text{C}-\text{H}$  bending/rocking, and  $\text{C}-\text{H}$  stretching were detected around  $1400$ – $1500$ ,  $1300$ – $1400$ , and  $2950 \text{ cm}^{-1}$ , respectively. A high-intensity broad peak corresponding to adsorbed water was observed around  $3300 \text{ cm}^{-1}$ , characteristic of a hydrophilic solid. The CST $n$  composite displayed a major band below  $1000 \text{ cm}^{-1}$ , which was assigned to the  $\text{Ti}-\text{O}-\text{Ti}$  framework vibrational mode observed in pure titania [41]. The anchoring of  $\text{TiO}_2$  weakened the peak intensities of carboxyl ( $1705 \text{ cm}^{-1}$ ) and hydroxyl ( $1100$ – $1300 \text{ cm}^{-1}$ ) groups present in CS. This decrease occurred progressively with increasing  $\text{TiO}_2$  content (or lowering  $n$  value), indicating that these functional groups were consumed by reacting with  $\text{TiO}_2$ . Sufficiently increasing the  $\text{TiO}_2$  content and thus lowering  $n$  below 3 in CST $n$  attenuated all absorption intensities from residual CS surface groups, implying that a  $\text{TiO}_2$  shell of adequate thickness completely covered CS.

Fig. 4 compares the XPS spectra of CST3, CS, and the control pure titania (TO3). The CST3 composite and TO3 presented the same  $\text{Ti} 2\text{p}$  ( $\text{Ti} 2\text{p}_{1/2}$ ,  $2\text{p}_{3/2}$  at  $465.1$  and  $459.3 \text{ eV}$ , respectively) and  $\text{O} 1\text{s}$  ( $530.5 \text{ eV}$ ) peaks. However, their  $\text{O} 1\text{s}$  peak appeared at a different position from that of CS, indicating that only oxygen atoms in  $\text{TiO}_2$  shells measuring several hundred nm in thickness in CST3 were detected by XPS [42,43]. This indirectly confirms that the nanoscale-thickness  $\text{TiO}_2$  shell perfectly surrounded the CS surface in CST3. The deconvolution of the  $\text{C} 1\text{s}$  peak of CS identified surface species similar to those obtained by FT-IR (Table S3), quantitatively showing the existence of aromatic ( $\text{sp}^2$ )  $\text{C}=\text{C}$  ( $8.4\%$ ,  $284.6 \text{ eV}$ ),  $\text{sp}^3$   $\text{C}-\text{C}$  ( $44.5\%$ ,  $285.2 \text{ eV}$ ),  $\text{C}-\text{OH}/\text{C}-\text{O}-\text{C}$  ( $31.3\%$ ,  $286.3 \text{ eV}$ ),  $\text{C}=\text{O}$  ( $12.7\%$ ,  $287.7 \text{ eV}$ ), and  $\text{O}=\text{C}-\text{O}$  linkages ( $3.2\%$ ,  $289.5 \text{ eV}$ ) [43–45]. The  $\text{sp}^3$   $\text{C}-\text{C}$  bond exhibited a greater fraction than the  $\text{sp}^2$   $\text{C}=\text{C}$ , suggesting that the CS core may comprise a more hydrophobic  $\text{sp}^2$   $\text{C}=\text{C}$  inner part and an  $\text{sp}^3$   $\text{C}-\text{C}$  aliphatic outer moieties which are related to the hydrophilic  $\text{C}-\text{OH}$ ,  $\text{C}-\text{O}-\text{C}$ , and  $\text{O}=\text{C}-\text{O}$  groups because it is reasonable that these hydrophilic groups would like to present on the CS outer surface so as to adapt to the polar water environment in the preparation solution. Moreover, CST3 showed a much weaker

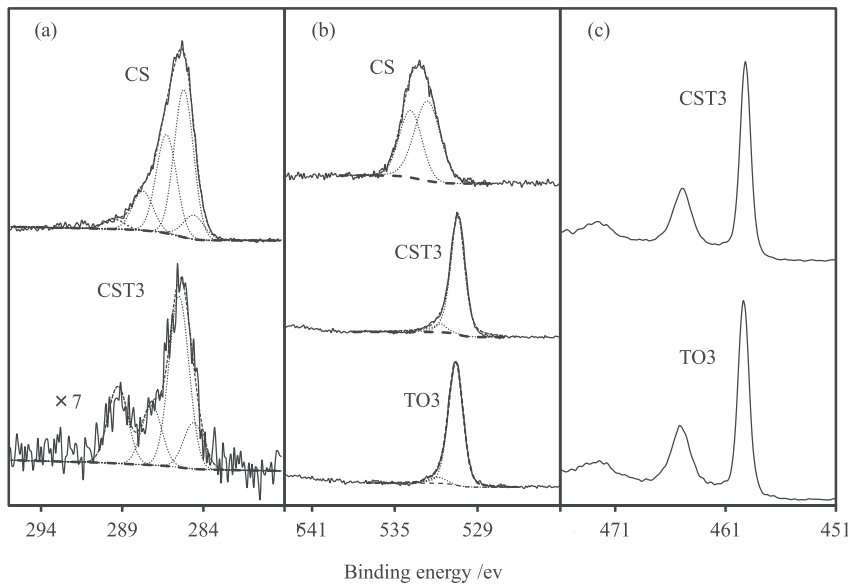


Fig. 4. (a) C 1s, (b) O 1s, and (c) Ti 2p XPS spectra of CST3, CS, and TO3.

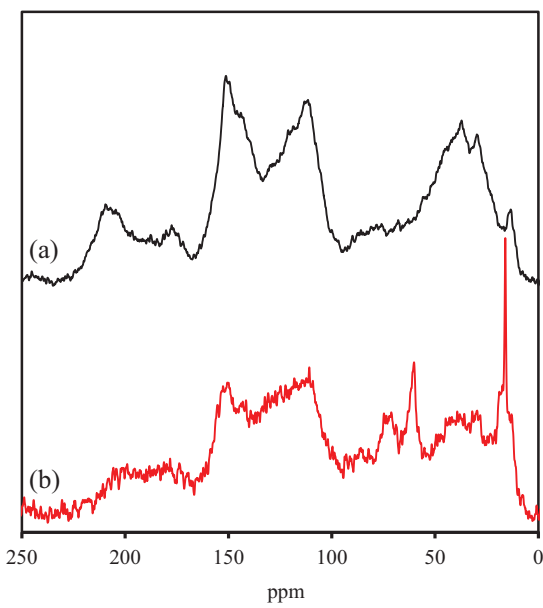


Fig. 5.  $^{13}\text{C}$  CP-MAS NMR spectra of (a) CS and (b) CST3. The spinning rates of the samples were 10 kHz.

C 1s signal than CS, consistent with the thick anchored  $\text{TiO}_2$  shell. The deconvolution of the C 1s peak of CST3 showed only  $\text{O}=\text{C}-\text{O}$  and  $\text{C}=\text{O}$  groups (Table S3), indicating that these surface groups were positioned on the outermost surface of CS. An increase in carbonization level (a higher  $\text{C}=\text{C}$  and  $\text{C}-\text{C}$  fractions) of CST3 (Table S3) suggests that CS possibly undergoes structural changes when reacting with the hydrolyzed titanium species during the second HTT. These phenomena will be discussed further in terms of NMR data below.

NMR has been proven powerful for probing solid bulk structure. Based on a comprehensive study using various advanced NMR techniques, Baccile et al. proposed a structural model for glucose-derived CS, in which the basic skeleton comprised a keto-aliphatic chain cross-linking aromatic furan ring backbone instead of a graphene-like framework [31,46,47]. As shown in

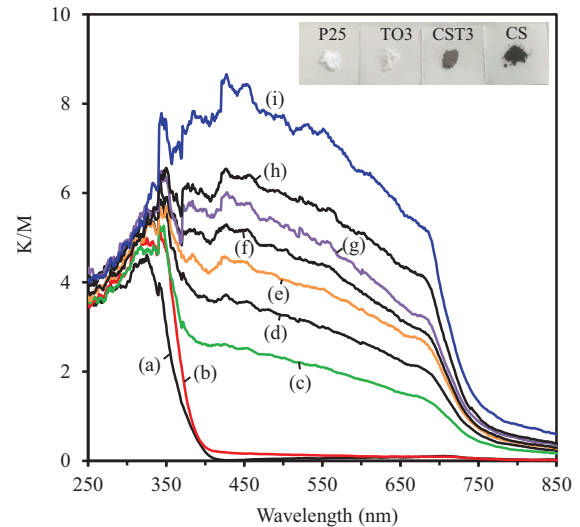
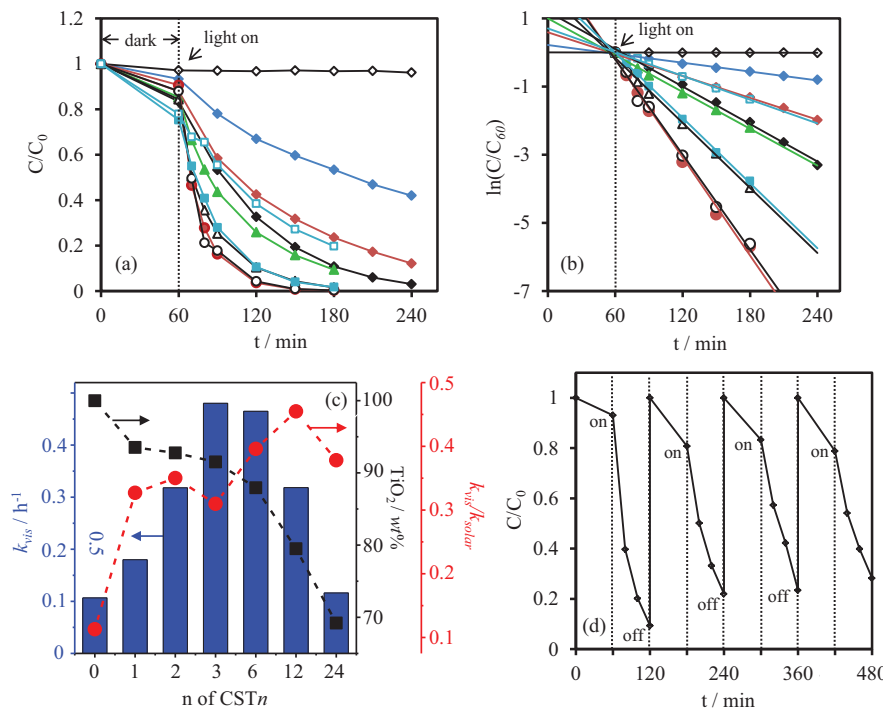


Fig. 6. UV-vis DRS of (a) P25, (b) TO3, CST $n$  with  $n$ =(c) 1, (d) 2, (e) 3, (f) 6, (g) 12, and (h) 24, and (i) CS.

Fig. 5, the sucrose-derived CSs exhibited extremely similar cross-polarization magic angle spinning (CP-MAS)  $^{13}\text{C}$  NMR spectrum to that of the glucose one. Therefore, these NMR signals were assigned according to the previous report [46], which corresponded to  $\beta(3)\text{-C}$  (111 ppm) and  $\alpha(4)\text{-C}$  (142 and 151 ppm) in the furan ring,  $\text{C}=\text{O}$  (208 ppm) in the keto-aliphatic cross-linker,  $-\text{CH}_3$  (13.2 ppm), mobile and rigid  $-\text{CH}_2$  (30 and 37 ppm) groups, and the  $\text{COOH}$  group (178 ppm) (refer to Fig. S9 too). Signals for aromatic OH groups, which were detected by FT-IR, appeared in the 100–130 ppm region, overlapping with the peak for the  $\beta(3)\text{-C}$  (111 ppm) of the furan ring. Spectral changes between CST3 and the original CS account for the structural modification of CS during the second HTT. The characteristic change upon the formation of CST3 was the appearance of new peaks for  $\text{C}-\text{OH}$  (72.6 ppm),  $\text{C}-\text{O}-\text{C}$  (60 ppm), and  $\text{CH}_3$  (16 ppm) groups. Sharper peaks were observed for  $\text{C}-\text{O}-\text{C}$  and, especially, for  $\text{CH}_3$  groups, indicative of the mobile property of these newly formed species. Despite the weaker signals due to the less carbon content in CST3 compared



**Fig. 7.** (a, b) Time courses of MO degradation under visible light (>400 nm) irradiation by CST<sub>n</sub> with  $n=1$  (▲), 2 (△), 3 (●), 6 (○), 12 (■), 24 (□) in comparison with those by TO3 (◆), P25 (◆), CS (◊), and GT<sub>0.1</sub> (◆) (catalysts: 20 mg for all test, MO: 1 ppm, 100 mL); (c) relationship of  $k_{vis}$  (blue bar), TiO<sub>2</sub> content (■), and  $k_{vis}/k_{solar}$  (●) with  $n$  of CST<sub>n</sub> (where  $n=0$  represents TO3), and (d) repeating degradation of MO by CST3 under visible light (>400 nm) irradiation.

to CS, one can observe that the anchoring of TiO<sub>2</sub> also intensified peaks corresponding to carboxyl (178 ppm) and aromatic C—O (100–130 ppm) groups, and caused their chemical shifts to move downfield, which can be attributed to the formation of O=C—O—Ti and C—O—Ti linkages or aromatic rings.

The as-prepared CS displayed a nonporous nature, whereas the composite CST<sub>n</sub> exhibited a mesoporous structure by nitrogen adsorption porosimetry (Fig. S10). For  $n < 4$ , the composite CST<sub>n</sub> presented higher total, internal (mesopore) specific surface area, and pore volume but a smaller average pore diameter than bare TiO<sub>2</sub> by t-plot analysis (Table S4) [48]. Moreover, the porosity of CST<sub>n</sub> increased reasonably with increasing TiO<sub>2</sub> content and reached a maximum for  $n \leq 3$ .

### 3.3. DRS and photocatalytic behaviors

Although TiO<sub>2</sub> nanoparticles completely covered CS in the TiO<sub>2</sub>@CS structure, the CS core plays an important role in the light absorption of the composite. UV-vis DRS (Fig. 6) revealed that the dark brown bare CS exhibited a broad absorption band ranging from 250 to 700 nm and centered around a maximum at 460 nm, spanning the entire visible light range (400–700 nm). In contrast, TO3 and P25 mainly absorbed light below 400 nm because of their greater band gap energy (~3.1 and ~3.0 eV, respectively, as shown in Fig. S18), although TO3 also showed a slight absorption at the longer wavelength range (>400 nm). This clearly demonstrated that the spectrum obtained for CST<sub>n</sub> combined the optical properties of titania and CS. Also, the contribution of CS to visible light absorption increased with increasing CS content in TiO<sub>2</sub>@CS. The light absorption properties of the materials were consistent with their colors, i.e., the dark brown CS, the dark gray CST3, the light gray TO3, and the white P25 (inset, Fig. 6). The deeper color of TO3 relative to the white P25 was reflected by the slightly enhanced light absorption of TO3 around 400–500 nm, indicating that lattice

defects may be generated during the hydrothermal synthesis of TO3.

The DRS results showed that TiO<sub>2</sub>@CS simultaneously benefited from the light absorption properties of TiO<sub>2</sub> surface and CS core. In this study, we consider that CS enhances the photocatalytic activity of the anchored TiO<sub>2</sub> by improving its visible light absorbing range. Therefore, TiO<sub>2</sub>@CS can drive an efficient photocatalysis under visible light irradiation. Here its visible light photocatalytic activity was evaluated toward the degradation of methyl orange (MO), bisphenol A (BPA), and oseltamivir phosphate (OP) in aqueous media. While MO is a typical industrial dye pollutant, the endocrine or hormone disruptor BPA is a persistent organic pollutant (POP) discharged as wastes by plastics industries. Better known through its trade name Tamiflu®, the anti-influenza medicine OP has recently raised concern as a kind of newly evolved pharmaceutical and personal care products (PPCPs) that may cause the evolution of antiviral drug resistant genes and viruses [49,50]. Figs. 7 and 8 show the photodegradation behaviors of MO, BPA, and OP. A small amount of pollutant molecules was adsorbed during an initial adsorption (dark) step that takes a 1/2–1 h to reach equilibrium. Once the photoexcitation was turned on, pure CS did not show any notable degradation toward MO (Fig. 7a). Concurrently, the CST<sub>n</sub> materials degraded MO more efficiently than TO3 and P25 (Fig. 7a). Therefore, the CS core indeed enhanced the visible light photoactivity of the anchored TiO<sub>2</sub>. In addition, some of the CST<sub>n</sub> materials exhibited greater photodegradability than TO3 not only under visible light but also under UV light-containing simulated solar irradiation (Fig. S11). Depending on synthesis conditions, they displayed significantly higher degradation efficiency than the graphene-titania composites (GT<sub>x</sub>), which have recently attracted high interest (see Section 2 of Supporting Information and Fig. S12 for the optimization of the GT<sub>x</sub> composites). The efficiency of MO degradation under visible light irradiation relies on the CS/Ti ratio of CST<sub>n</sub>. It increased with changing  $n$  from 1 to 6 but decreased beyond  $n=12$  (Fig. 7a). Conducting HTT above 418 K is

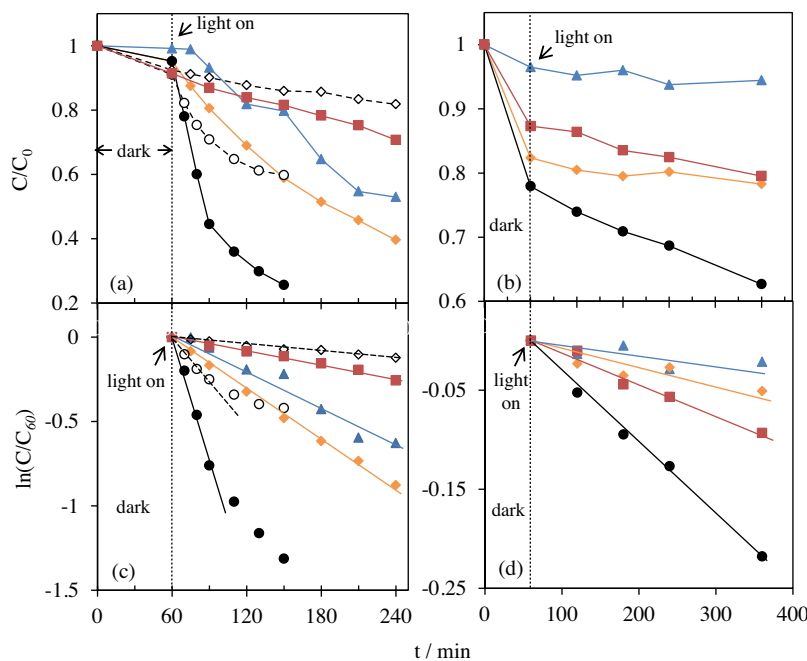


**Fig. 8.** Photodegradation time courses of (a, b) BPA and (c, d) OP under visible light ( $> 400$  nm) irradiation by CST3 (●), GT<sub>0.1</sub> (■), TO3 (◆), and P25 (▲) in pure water, and CST3 (○) and TO3 (◊) in tap water. 20 mg catalysts and 5 ppm BPA or OP in 50 mL were used for all the tests.

another prerequisite for achieving maximum performance because this treatment determines the TiO<sub>2</sub> nanocrystal structure (Fig. S4 and S13). Moreover, the faster photodegradation speed by TO3 as compared to P25 is owing to deficient sites in TO3, as demonstrated by a slight enhancement in absorption around 400–500 nm (Fig. 6 and ESR results below).

The photodegradation rate of MO is further estimated using the *pseudo* first-order kinetic equation [51]:

$$\ln(C/C_{60}) = -kt \quad (1)$$

where  $C_{60}$  and  $C$  are the organic molecule concentrations at the beginning of illumination (or end point of the dark adsorption step) and illumination time  $t$ , respectively, and  $k$  is the *pseudo* first-order rate constant. The  $k$  values for MO degradation under visible light ( $k_{vis}$ ) and simulated solar ( $k_{solar}$ ) irradiation were calculated using the linear relationship between  $\ln(C/C_{60})$  and  $t$  (Fig. 7b, S11b, and Table S5). Fig. 7c illustrates the relationship of  $k_{vis}$ , the  $k_{vis}/k_{solar}$  ratio, and the TiO<sub>2</sub> content of CST<sub>n</sub> as a function of  $n$ . It is plausible that the  $k_{vis}$  value reaches a peak at  $n = 3$ , where it is  $\sim 5$ ,  $\sim 10$ , and  $\sim 2.6$  folds greater than those of TO3 containing only TiO<sub>2</sub>, the commercial P25, the GT<sub>0.1</sub>, respectively, and is approximately 30% of the  $k_{solar}$  value. The  $k_{vis}/k_{solar}$  ratio of CST<sub>n</sub> with a higher  $n$  ( $n > 6$ ), which is the condition for the presence of a smaller amount of TiO<sub>2</sub> NPs in a greater amount of CS that favors sufficient contacting of TiO<sub>2</sub> NPs with CS, appears to be higher than those of CST<sub>n</sub> with  $n < 3$ . Because a decrease of  $n$  from 24 to 3 favors the formation of a perfect TiO<sub>2</sub>@CS structure by providing more TiO<sub>2</sub> around the CS surface (Fig. 3), the further decrease of  $n$  at  $n < 3$  in the synthesis mainly contributes to the thickening of the TiO<sub>2</sub> shell or to the increase of the amount of TiO<sub>2</sub> NPs apart from the CS core at the outer surface of the shell. Therefore, the results demonstrate that the interfacial contacting structure of TiO<sub>2</sub> and CS in the form of TiO<sub>2</sub>@CS is a key factor responsible for the visible light photoactivity. Note that the amount of TiO<sub>2</sub> (80–93 wt%) that achieves the highest performance in CST<sub>n</sub> is also less than those in GT<sub>x</sub> in addition to the unfavorable lower efficiency and the time- and cost-consuming processes of precursor synthesis required for the latter. The better photocatalytic performance of TiO<sub>2</sub>@CS as compared to other samples

was also observed at a higher MO initial concentration (Fig. S14), and this phenomenon was more evident when longer wavelength excitation was employed (Fig. S15). Moreover, the repeatability of visible light photocatalytic activity of CST3 was quite good as shown in Fig. 7d.

Despite the different ionic properties of the anionic MO, the nondissociative hydrophobic BPA, and the zwitterion OP pollutant molecules in neutral media [50], the TiO<sub>2</sub>@CS materials can advantageously drive the visible light photodegradation not only for MO but also for BPA and OP. As shown in Fig. 8 and Table S6, the  $k_{vis}$  values of CST3 are enhanced by more than four, five and fifteen times for BPA and by about five, nine and two and a half times for OP as compared to TO3, P25 and GT<sub>0.1</sub>, respectively. Interestingly, the visible light-excited photocatalysis of BPA by CST3 is maintained, albeit with a decreased effect, even in experiments using tap water as the aqueous media while the same condition almost deactivates TO3. Because tap water is a media containing many interfering matrix organics (e.g., the polar humic and fulvic acids or others) [52], this result reveals that the TiO<sub>2</sub>@CS structure suffers less interference from matrix organics compared to the pure TiO<sub>2</sub> NPs. This superior selectivity makes the TiO<sub>2</sub>@CS materials more feasible for utilization in practical sewage or drinking water treatment.

### 3.4. Photocurrent responses and ESR

The above results clearly show that the interfacial contacting of TiO<sub>2</sub> and CS by constructing TiO<sub>2</sub>@CS structure at an optimum condition is a novel and facile way to achieve visible light photoactivity with stability and selectivity. To further elucidate the photocatalytic mechanism, photocurrent response experiment and electron spin resonance (ESR) technique were employed. Transient photocurrent responses are the straightforward reflections of excitation, separation, and transfer of the photogenerated charge carriers. As demonstrated in Fig. 9a, as is typical of the *n*-type semiconductors, the pure P25 and TO3 exhibit a strong anodic photocurrent response under illumination by the full spectrum of light due to the charge transfer between the VB and CB of TiO<sub>2</sub>. The larger

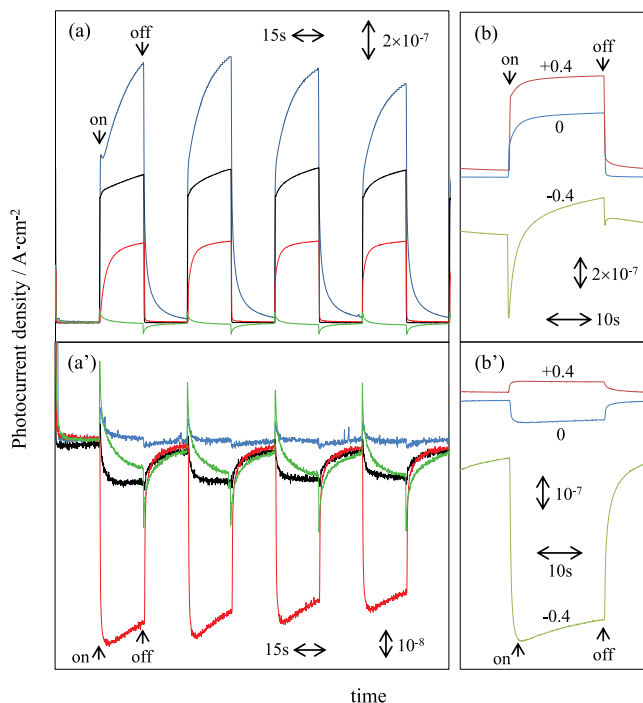


**Fig. 9.** Photocurrent responses of (a, a') CST3 (red), CS (green), TO3 (black), and P25 (blue) at zero bias voltage and (b, b') those of CST3 at various bias voltages under simulated solar (a, b) and visible light ( $>400$  nm) (a', b') excitations. (For interpretation of the references to colour in this figure legend, the reader is referred to the web version of this article.).

photocurrent of P25 is due to the greater amount of photogenerated carriers. Compared to TO3 and P25, CST3 shows a small photocurrent response that is indicative of a smaller amount of conductive electrons. CS is almost not photosensitive to the excitation by the full light spectrum. Conversely, photocurrent responsivity is completely different when the materials are irradiated by visible light (the simulated solar light with a cut-off filter  $<400$  nm). As shown in Fig. 9a', while P25 loses its photosensitivity in this case, CST3 changes to *p*-type semi-conductivity with a cathodic photoresponsive current (the reverse direction of the anodic one), implying that the holes ( $h^+$ ) rather than electrons flow into the electrode from the material [13,23,53]. This phenomenon underlies the different charge (carriers) generation and tuning mechanisms of CST3 compared to those of the pure  $TiO_2$ . Because the CST3 photocurrent changes direction upon the tuning of the bias voltage from positive to negative and vice versa (Fig. 9b, b'), it is clear that both *n* and *p* type photoresponsive processes are present in the  $TiO_2@CS$  structure, resulting in a tunable total sum photocurrent. The dependency of cathodic photoresponsivity of CST3 on the excitation wavelength shows that the photoresponse is the highest at blue light (450 nm) excitation; progressively decreases with the red-shifting of the excitation from blue to red; and is even traceable at the red light (650 nm) excitation (Fig. S16a, S16a'), coinciding well with the broad visible absorption property (Fig. 6). Thus, it is indeed the visible light that induces the *p*-type (cathodic) photocurrent and accordingly the visible light photocatalytic activity. Because the anodic photocurrent usually originates from the UV ( $<400$  nm)-induced photo electrons in CB of  $TiO_2$ , the appearance of anodic photocurrent at a positive bias voltage (+0.4 V) indicates the existence of doping levels at the interface of  $TiO_2$  and CS for which the charge separation can be activated by visible light excitation (Fig. 9b'). Examination of the effect of the excitation wavelength (Fig. S16c) proves that the major fraction of the interfacial doping levels are distributed immediately above (0.1–0.25 eV, equivalent

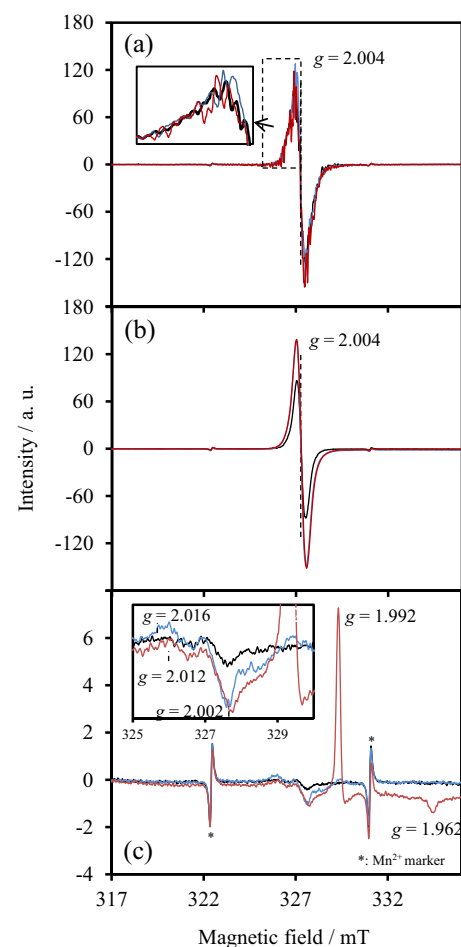


**Fig. 10.** ESR spectra of (a) CS, (b) CST3, and (c) TO3 measured at 77 K without excitation (black) and under visible ( $>400$  nm, blue) and full spectrum (red) light excitations. (For interpretation of the references to colour in this figure legend, the reader is referred to the web version of this article.)

to 400–420 nm, higher than) the VB of  $TiO_2$ . We also observed the cathodic current response of TO3 under visible light but with a much smaller current density (Fig. 9a'). Unlike CST3, TO3 does not strongly respond to excitations at wavelengths above 450 nm (Fig. S16b, S16b'). The *p*-type photocurrent response of TO3 therefore arises from  $h^+$  carriers formed by charge transfer between the VB of TO3 and certain kinds of oxygen vacancy sites with an energy level slightly lower than CB, which can be excited by a light beam at 400–450 nm (an equivalent of approximately 2.76–3.2 eV). The charge transfer mechanism of this kind agrees with the slightly increased absorption of TO3 at 400–450 nm relative to that of P25 (Fig. 6). Moreover, a slight and slow photocurrent response carried by  $h^+$  is also observed for the bare CS that, however, is not connected with an improved photocatalytic activity.

As evidenced by the photodegradation of organic pollutants and the photocurrent, the embedding of CS in the form of  $TiO_2@CS$  results in a photoinduced process that differs from those of P25 and the bare TO3 and substantially enhances the photoactivity and cathodic photocurrent response of  $TiO_2$  under visible light excitation. The information provided by ESR can further assist the understanding of such an enhancement mechanism. Fig. 10 compares the ESR spectra of CS, CST3, and TO3 without and with (full spectrum or visible light) excitations. A strong ESR signal is observed for CS with a *g*-value of 2.004 in air atmosphere without any external excitation (Fig. 10a) [54]. CS displays a hyperfine splitting in its ESR spectrum superimposed on the original broad

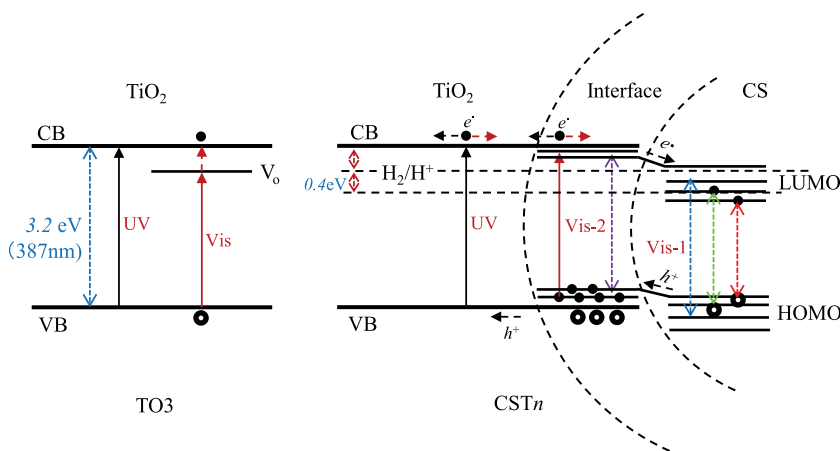


**Fig. 11.** Proposed mechanism for the photoinduced charge separation of carbon sphere-TiO<sub>2</sub> composite (CSTn) and the pure titania (TO3).

symmetric signal, implying that part of unpaired electrons are localized in a complex chemical environment such as the keto-aliphatic chain-linked furan backbone-like structure in CS. The ESR signal is not changed by the excitation of either the full spectrum light or the visible light. This fact is consistent with the noble photocatalytic activity of CS. Conversely, CST3 displays a symmetric ESR signal with minimal hyperfine splitting at the same  $g=2.004$  (Fig. 10b), indicating the change of chemical environment of unpaired electrons in CS after composing with titania. Upon visible light irradiation, a different ESR signal was superimposed on the original ESR signal. This additional paramagnetic species corresponds to the enhancement of cathodic photocurrent and photocatalysis by visible light excitation. The similar behavior has been reported previously and was attributed to the charge transfer between the carbon atoms and TiO<sub>2</sub> [55,56]. Upon full spectrum light irradiation, the ESR signal is also enhanced whereas it has an identical shape and intensity with that under visible light irradiation. It is well known that UV-irradiated anatase generates both signals of Ti<sup>3+</sup> ( $g_{\perp} \sim 1.990$ ,  $g_{\parallel} \sim 1.960$ ) and oxygen-related hole trapped center ( $g_1 \sim 2.002$ ,  $g_2 \sim 2.012$ ,  $g_3 \sim 2.016$ ) [57]. The absence of Ti<sup>3+</sup> signal in the ESR spectrum of CST under full spectrum light further evidences the charge transfer between the TiO<sub>2</sub> shell and the CS core which makes the UV-excited electrons to be stabilized in CS rather than CB of the TiO<sub>2</sub> shell. For TO3, while excitation by full spectrum light induces ESR signals of both Ti<sup>3+</sup> ( $g_{\perp}=1.992$ ,  $g_{\parallel}=1.962$ ) and hole trapped center ( $g_1=2.002$ ,  $g_2=2.012$ ,  $g_3=2.016$ ), that by visible light only generates the signal of hole trapped center. The result implies the trapping of electrons in oxygen vacancies of TO3 under visible light excitation [58,59] which can slowly diffuse into CB of TiO<sub>2</sub> as evidenced by the appearance of an evident Ti<sup>3+</sup> signal after a longer measurement time (Fig. S17). This process is responsible for the visible light photoactivity of TO3 and the *p*-type photocurrent under visible light with respective to the usual *n*-type one under full spectrum light. Therefore, the above results clearly confirm the different charge transfer mechanism of TiO<sub>2</sub> shell with and without a counterpart of carbon core.

### 3.5. Charge separation mechanism

In summary, the photoinduced charge separation mechanism for TiO<sub>2</sub>@CS is schematically described and compared with that for TO3 in Fig. 11. For TO3, some oxygen vacancies (V<sub>o</sub>) were formed in the hydrothermal synthesis process which is a condition of lower temperature and insufficient oxygen atmosphere compared to the

high temperature pyrolysis approach. While the band gap energy of TO3 was calculated to be 3.1 eV from UV-vis spectra (Fig. S18) [60], the energy level of V<sub>o</sub> is estimated to be 0.3–0.6 eV lower than that of the CB of TiO<sub>2</sub> because photocurrent mainly responds to visible light in the range below 500 nm (Fig. S16 b, b'). Thus, there exist a usual pathway (UV) in which the charge transfer occurs between the VB and CB of TiO<sub>2</sub> by full spectrum photoexcitation, leading to a typical *n*-type anodic current, and another pathway (Vis) in which e<sup>-</sup> is excited by visible light to V<sub>o</sub>, leaving the h<sup>+</sup> in VB to promote a cathodic current. The latter Vis pathway accounts for the visible light photocatalytic activity. Identification of a weak Ti<sup>3+</sup> signal in the longer time ESR measurement indicates that it is possible for the electrons excited to V<sub>o</sub> site to slowly diffuse to the CB of TiO<sub>2</sub> (Fig. S17).

Unlike for TO3, a close-contacting interfacial structure is built up between TiO<sub>2</sub> shell and CS core in TiO<sub>2</sub>@CS, to which the free radical species in the pristine CS are tuned to produce the doping levels mainly distributed at an energy level 0.1–0.25 eV (400–420 nm equivalent) higher than the VB of TiO<sub>2</sub> (Fig. S16c). This situation is similar to that of a graphene-TiO<sub>2</sub> composite where the tuning of electrons from a graphene sheet to a rutile (110) surface generates a doping level albeit with a higher energy (0.5–0.65 eV higher than the VB of TiO<sub>2</sub>) as reported previously [61]. As the result, the unpaired electrons in the pristine CS are localized in a more uniform chemical environment, due to which the hyperfine structure of the ESR signal almost disappeared (Fig. 10). Such an electron donation (oxidation) process of CS that also partially changes the CS structure (Fig. 5), means that CS can link with TiO<sub>2</sub> through a certain kind of chemical bonding such as C–O–Ti (Fig. 3) so that the CS core correlates to the interfacial structure of TiO<sub>2</sub>@CS with the highest occupied molecular orbital (HOMO) level more oxidized (with a lower energy) relative to the doping level. Similarly, the LUMO level of CS is located at a lower energy relative to the CB (or the nearby doping levels) of TiO<sub>2</sub> as determined by the visible light absorption property of CS (Fig. 6). Thus, three pathways exist in the TiO<sub>2</sub>@CS structure: the usual UV-excited pathway (UV) that transfers electron from the VB to the CB in the TiO<sub>2</sub> shell, the visible light-excited pathway (Vis1) that leads to the charge transfer between the HOMO and LUMO of the CS core, and the pathway (Vis2) that excites the electrons from the doping levels to the CB of TiO<sub>2</sub> in the interfacial structure. Obviously, the Vis1 pathway showing the highest efficiency at blue to green light range is primarily responsible for the remarkable cathodic photocurrent (Fig. 9) and the enhanced visible light photocatalytic activity (Figs. 7 and 8). By contrast, the Vis2 and UV pathways are most effective only for

the excitations near (400–420 nm) and below 400 nm (Fig. S16), respectively. Due to the peculiar interfacial structure in  $\text{TiO}_2@\text{CS}$ , the photoexcited electrons in the Vis2 and UV pathways can diffuse either toward the outside of the  $\text{TiO}_2$  shell or toward the inside of the CS core, thus contributing either to the anodic or to the cathodic current depending on the external bias voltage (Fig. 9). The lower energy level LUMO of CS in the proposed interfacial structure also serves as the trapping site to sink the photoexcited electrons through the UV and Vis2 pathways in the low temperature ESR experiment, thus disabling the detection of the  $\text{Ti}^{3+}$  species (Fig. 10). The multiple pathways of charge transfer and diffusions thereby promote electron-hole separation and accelerate the photocatalytic performance of the  $\text{TiO}_2@\text{CS}$  under both visible and solar light illuminations.

The above discussions unearthed the underlying mechanism that has not been made clear in the previous reports, for example, on the mortar-and-brick-type material despite that a dyad hybridized structure was proposed [23]. The proposed mechanism resembles but seems unnecessarily the same with that of the hetero-junction hybridized structure where a depletion layer is formed by the cross diffusions of carriers at the interface of two semiconductors [62]. The mechanism based on our obtained evidence strongly favors the important role of interfacial structure in the enhancement of photocatalysis and photocurrent behaviors. The higher visible photocatalytic activity of  $\text{TiO}_2@\text{CS}$  as compared to graphene- $\text{TiO}_2$  composite is then attributable to the perfect core-shell structure which leads to more interfacing sites to facilitate charge separation. Therefore, we conclude that a path for easy access to a visible light active photocatalyst with a high efficiency but low cost can be carved out by enabling an interface charge transfer mechanism between the  $\text{TiO}_2$  shell and CS core through the construction of a  $\text{TiO}_2@\text{CS}$  structure.

#### 4. Conclusion

A series of  $\text{TiO}_2@\text{CS}$  materials are successfully fabricated using the hydrothermal method in the ethanol phase containing a small fraction of water, with structures dependent on the water content, temperature, and CS/ $\text{TiO}_2$  weight ratio employed in the synthesis. A nanoscale layer of anatase-typed  $\text{TiO}_2$  nanoparticles are condensed and coated over the CS surface to form an interfacial structure through which the CS core can enhance the light absorbing ability of  $\text{TiO}_2$ . The MO, BPA, and OP photodegradation experiments demonstrate that the  $\text{TiO}_2@\text{CS}$  material is highly visible light active compared to the pure  $\text{TiO}_2$  and the well-known graphene- $\text{TiO}_2$  composite material. Detailed examinations of photocurrent response and ESR signals confirm the interfacial doping levels formed by electron tuning from the CS core to the  $\text{TiO}_2$  shell and disclose a sophisticated photocatalytic mechanism involving the CS core, CS- $\text{TiO}_2$  interface, and  $\text{TiO}_2$  shell. The  $\text{TiO}_2@\text{CS}$  materials are easy to fabricate, inexpensive, and nontoxic, endowing them with a considerable potential for applications in UV-free photocatalysis.

#### Acknowledgements

The authors acknowledge the financial support from the Japan Society for the Promotion of Science. This work was partly supported by the AIST Water Project. AIST Nanocharacterization Facility and TEM/SEM Facility of the Innovation Boosting Equipment Common platform within the “Nanotechnology Platform” of the Japanese Ministry of Education, Culture, Sports, Science and Technology are grateful for providing equipments and technical assistances.

#### Appendix A. Supplementary data

Supplementary data associated with this article can be found, in the online version, at <http://dx.doi.org/10.1016/j.apcatb.2017.02.027>.

#### References

- [1] A. Fujishima, K. Honda, *Nature* 238 (1972) 27–38.
- [2] H. Park, H. Kim, G. Moon, W. Choi, *Energy Environ. Sci.* 9 (2016) 411–433.
- [3] J. Schneider, M. Matsuoka, M. Takeuchi, J. Zhang, Y. Horiuchi, M. Anpo, D.W. Bahnemann, *Chem. Rev.* 114 (2014) 9919–9986.
- [4] H. Li, Y. Zhou, W. Tu, J. Ye, Z. Zou, *Adv. Funct. Mater.* 25 (2015) 998–1013.
- [5] L. Wang, S. Liu, Z. Wang, Y. Zhou, Y. Qin, Z.L. Wang, *ACS Nano* 10 (2016) 2636–2643.
- [6] A. Fujishima, X. Zhang, D.A. Tryk, *Surf. Sci. Rep.* 63 (2008) 515–582.
- [7] H. Dong, G. Zeng, L. Tang, C. Fan, C. Zhang, X. He, Y. He, *Water Res.* 79 (2015) 128–146.
- [8] S. Banerjee, S.C. Pillai, P. Falaras, K.E. O’shea, J.A. Byrne, D.D. Dionysiou, *J. Phys. Chem. Lett.* 5 (2014) 2543–2554.
- [9] H. Barndök, D. Hermosilla, C. Han, D.D. Dionysiou, C. Negro, Á. Blanco, *Appl. Catal. B: Environ.* 180 (2016) 44–52.
- [10] J.S. Lee, K.H. You, C.B. Park, *Adv. Mater.* 24 (2012) 1084–1088.
- [11] Z. Zhang, L. Zhang, M.N. Hedihi, H. Zhang, P. Wang, *Nano Lett.* 12 (2013) 14–20.
- [12] C. Dette, M.A. Pérez-Ororio, C.S. Kley, P. Punke, C.E. Patrick, P. Jacobson, F. Giustino, S.J. Jung, K. Kern, *Nano Lett.* 14 (2014) 6533–6538.
- [13] C. Chen, W. Cai, M. Long, B. Zhou, Y. Wu, D. Wu, Y. Feng, *ACS Nano* 4 (2010) 5425–5432.
- [14] Z. Jiang, C. Zhu, W. Wan, K. Qian, J. Xie, *J. Mater. Chem. A* 4 (2016) 1806–1818.
- [15] Y. Zhang, Z.-R. Tang, X. Fu, Y.-J. Xu, *ACS Nano* 5 (2011) 7426–7435.
- [16] K.M. Cho, K.H. Kim, H.O. Choi, H.-T. Jung, *Green Chem.* 17 (2015) 3972–3978.
- [17] M. Xing, X. Li, J. Zhang, *Sci. Rep.* 4 (2014) 5493.
- [18] Q. Xiang, J. Yu, M. Jaroniec, *Chem. Soc. Rev.* 41 (2012) 782–796.
- [19] L.-L. Tan, W.-J. Ong, S.-P. Chai, A.R. Mohamed, *Nanoscale Res. Lett.* 8 (2013) 465.
- [20] K. Woan, G. Pyrgiotakis, W. Sigmund, *Adv. Mater.* 21 (2009) 2233–2239.
- [21] W.J. Lee, J.M. Lee, S.T. Kochuveedu, T.H. Han, H.Y. Jeong, M. Park, J.M. Yun, J. Kwon, K. No, D.H. Kim, S.O. Kim, *ACS Nano* 6 (2012) 935–943.
- [22] K.R. Reddy, M. Hassan, V.G. Gomes, *Appl. Catal. A: Gen.* 489 (2015) 1–16.
- [23] L. Zhao, X. Chen, X. Wang, Y. Zhang, W. Wei, Y. Sun, M. Antonietti, M.-M. Titirici, *Adv. Mater.* 22 (2010) 3317–3321.
- [24] J. Zhang, Q. Tian, H. Zhou, Q. Liu, P. Liu, H. Zhong, *J. Mater. Chem.* 22 (2012) 7036–7042.
- [25] D. Zhao, G. Sheng, C. Chen, X. Wang, *Appl. Catal. B: Environ.* 111–112 (2012) 303–308.
- [26] L.-L. Tan, W.-J. Ong, S.-P. Chai, B.T. Goh, A.R. Mohamed, *Appl. Catal. B: Environ.* 179 (2015) 160–170.
- [27] X. Li, Y. Jiang, W. Cheng, Y. Li, X. Xu, K. Lin, *Nano-Micro Lett.* 7 (2015) 243–254.
- [28] H. Zhang, X. Lv, Y. Li, Y. Wang, J. Li, *ACS Nano* 4 (2010) 380–386.
- [29] F. Petronella, M.L. Curri, M. Striccoli, E. Fanizza, C. Mateo-Mateo, R.A. Alvarez-Puebla, T. Sibilano, C. Giannini, M.A. Correa-Duarte, R. Comparelli, *Appl. Catal. B: Environ.* 178 (2015) 91–99.
- [30] Y. Long, Y. Lu, Y. Huang, Y. Peng, Y. Lu, S.-Z. Kang, J. Mu, *J. Phys. Chem. C* 113 (2009) 13899–13905.
- [31] X. Sun, Y. Li, *Angew. Chem. Int. Ed.* 43 (2004) 597–601.
- [32] B. Hu, K. Wang, L. Wu, S.-H. Yu, M. Antonietti, M.-M. Titirici, *Adv. Mater.* 22 (2010) 813–828.
- [33] A.A. Deshmukh, S.D. Mhlanga, N.J. Coville, *Mater. Sci. Eng. R* 70 (2010) 1–28.
- [34] M.-M. Titirici, *Hydrothermal carbons: synthesis, characterization, and applications*, in: J.M.D. Tascoín (Ed.), *In Novel Carbon Adsorbents*, Elsevier, Oxford, 2012, pp. 351–399.
- [35] M.-M. Titirici, R.J. White, C. Falco, M. Sevilla, *Energy Environ. Sci.* 5 (2012) 6796–6822.
- [36] M.-M. Titirici, R.J. White, N. Brun, V.L. Budarin, D.S. Su, F. del Monte, J.H. Clark, M.J. MacLachlan, *Chem. Soc. Rev.* 44 (2015) 250–290.
- [37] C.-C. Nguyen, N.-N. Vu, T.-O. Do, *J. Mater. Chem. A* 4 (2016) 4413–4419.
- [38] R. Yang, H. Li, X. Qiu, L. Chen, *Chem. Eur. J.* 12 (2006) 4083–4090.
- [39] Y. Zhuang, J. Sun, M. Guan, *J. Alloys Compd.* 662 (2016) 84–88.
- [40] P. Zheng, H.-Y. Li, F. Wu, B. Bai, W.-S. Guan, *New J. Chem.* 39 (2015) 8787–8796.
- [41] V.A. Zeitler, C.A. Brown, *J. Phys. Chem.* 61 (1957) 1174–1177.
- [42] X. Chen, L. Liu, P.Y. Yu, S.S. Mao, *Science* 331 (2011) 746–750.
- [43] M.-C. Sun, J.-B. Liang, W.-Q. Peng, Z.-M. Wang, N. Negishi, K. Koike, Y.-H. Chu, H.-Q. Yin, *Mater. Sci. Semicond. Process* 40 (2015) 954–963.
- [44] J. Dou, S. Yin, J.Y. Chong, B. Zhang, J. Han, Y. Huang, R. Xu, *Appl. Catal. A: Gen.* 513 (2016) 106–115.
- [45] M. Li, W. Li, S. Liu, *Carbohydr. Res.* 346 (2011) 999–1004.
- [46] N. Baccile, G. Laurent, F. Babonneau, F. Fayon, M.-M. Titirici, M. Antonietti, *J. Phys. Chem. C* 113 (2009) 9644–9654.
- [47] R.-D. Cakan, N. Baccile, M. Antonietti, M.-M. Titirici, *Chem. Mater.* 21 (2009) 484–490.
- [48] B.C. Lippens, J.H. de Boer, *J. Catal.* 4 (1965) 319–323.

[49] W.-L. Wang, Q.-Y. Wu, Z.-M. Wang, H.-Y. Hu, N. Negishi, M. Torimura, *Chemosphere* 131 (2015) 41–47.

[50] W.-L. Wang, Q.-Y. Wu, Z.-M. Wang, L.-X. Niu, C. Wang, M.-C. Sun, H.-Y. Hu, *J. Environ. Manag.* 162 (2015) 326–333.

[51] C.G. da Silver, J.L. Faria, *J. Photochem. Photobiol. A: Chem.* 155 (2003) 13–143.

[52] Z.-M. Wang, H. Ooga, T. Hirotsu, W.-L. Wang, Q.-Y. Wu, H.-Y. Hu, *Appl. Clay Sci.* 104 (2015) 81–87.

[53] H. Chen, Q. Wang, M. Lyu, Z. Zhang, L. Wang, *Chem. Commun.* 51 (2015) 12072–12075.

[54] J. Zhang, G. Zhang, X. Chen, S. Lin, L. Möhlmann, G. Dolęga, G. Lipner, M. Antonietti, S. Blechert, X. Wang, *Angew. Chem. Int. Ed.* 51 (2012) 3183–3187.

[55] J. He, J. Zhao, H. Hidaka, N. Serpone, *Faraday Trans.* 94 (1998) 2375–2378.

[56] Z. Wang, W. Ma, C. Chen, H. Ji, J. Zhao, *Chem. Eng. J.* 170 (2011) 353–362.

[57] C.P. Kumar, N.O. Gopal, T.C. Wang, M.-S. Wong, S.C. Ke, *J. Phys. Chem. B* 110 (2006) 5223–5229.

[58] R.F. Howe, M. Grätzel, *J. Phys. Chem.* 91 (1987) 3906–3909.

[59] I. Nakamura, N. Negishi, S. Kutsuna, T. Ihara, S. Sugihara, K. Takeuchi, *J. Mol. Cat. A: Chem.* 161 (2000) 205–212.

[60] B. Ohtani, *Chem. Phys. Phys. Chem.* 16 (2014) 1788–1797.

[61] A. Du, Y.H. Ng, N.J. Bell, Z. Zhu, R. Amal, S.C. Smith, *J. Phys. Chem. Lett.* 2 (2011) 894–899.

[62] S.J.A. Moniz, S.A. Shevlin, D.J. Martin, Z.-X. Guo, J. Tang, *Energy Environ. Sci.* 8 (2015) 731–759.

Update

**Applied Catalysis B: Environmental**

Volume 269, Issue , 15 July 2020, Page

DOI: <https://doi.org/10.1016/j.apcatb.2019.118215>



Corrigendum

Corrigendum to “Anchoring titanium dioxide on carbon spheres for high-performance visible light photocatalysis” [Appl. Catal. B: Environ. 207 (2017) 255–266]



Haoyi Wu<sup>a</sup>, Xiao-Li Wu<sup>a,b</sup>, Zheng-Ming Wang<sup>a,\*</sup>, Hiroshi Aoki<sup>a</sup>, Shuzo Kutsuna<sup>a</sup>, Keiko Jimura<sup>c</sup>, Shigenobu Hayashi<sup>c</sup>

*Environmental Management Research Institute, National Institute of Advanced Industrial Science and Technology, 16-1 Onogawa, Tsukuba, Ibaraki 305-8569, Japan*

*College of Architecture and Environment, Sichuan University, No. 24 South Section 1, Yihuan Road, Chengdu 610065, Sichuan, PR China*

*Research Institute for Material and Chemical Measurement, National Institute of Advanced Industrial Science and Technology, 1-1-1 Higashi, Tsukuba, Ibaraki, 305-565, Japan*

The authors regret that there were some errors in the scale/dimension of the pseudo first-order rate constant  $k$ . On page 261, the correct dimension of  $k_{vis}$  (the left ordinate) in Fig. 7 (c) is  $(\times 1/10) \text{ min}^{-1}$ . In Supplementary Materials, the correct dimension of  $k$  values ( $k_1$ ,  $k_{vis}$ ,  $k_{solar}$ ,  $k_{vis}$ , BPA and  $k_{vis, op}$ ) in Figs. S14 and S15 and Tables S5 and S6 is  $\text{min}^{-1}$ . On page 256, section 2.1, the correct concentration for S dispersion (solution A) is  $5 \text{ mg}\cdot\text{mL}^{-1}$ . On page 258, in (a), (b), and (d)~(f) of Fig. 2, the scale number of 500 nm is missed for the scale bars.

On page 259, section 3.1, the major observed lattice fringes are (101) with  $d = 0.35 \text{ nm}$  but not (001). In Fig. 8, (a) and (c) are for BPA and, (b) and (d) are for OP. The correct page numbers of Ref. [13] are 6425–6432 and those of Ref. [51] are 133–143.

These corrections do not change the results and discussion of the original article. The authors would like to apologise for any inconvenience caused.

DOI of original article: <https://doi.org/10.1016/j.apcatb.2017.02.027>

\* Corresponding author: Environmental Management Research Institute, National Institute of Advanced Industrial Science and Technology, 16-1 Onogawa, Tsukuba, Ibaraki, 305-8569, Japan.

E-mail address: [zm-wang@aist.go.jp](mailto:zm-wang@aist.go.jp) (Z.-M. Wang).